Three-dimensional electrode arrays for retinal prostheses: modeling, geometry optimization and experimental validation

Three-dimensional electrode arrays for retinal prostheses: modeling, geometry optimization and experimental validation

M Djilas[1,2,3,12]**, C Olès**[1,2,3]**, H Lorach**[1,2,3]**, A Bendali**[1,2,3]**, J Dégardin**[1,2,3]**,
E Dubus**[1,2,3]**, G Lissorgues-Bazin**[4]**, L Rousseau**[4]**, R Benosman**[1,2,3,5]**,
S-H Ieng**[5]**, S Joucla**[6,7]**, B Yvert**[6,7]**, P Bergonzo**[8]**, J Sahel**[1,2,3,9,10,11] **and
S Picaud**[1,2,3,11]

[1] INSERM, U968, Institut de la Vision, Paris, France
[2] Institut de la Vision, UPMC Université Paris 6, UMR_S968, Paris, France
[3] CNRS, UMR 7210, Institut de la Vision, Paris, France
[4] ESIEE, Université Paris Est, Noisy le Grand, France
[5] ISIR, Université Pierre et Marie Curie, Paris, France
[6] Centre National de la Recherche Scientifique, INCIA, UMR5287, Bordeaux, France
[7] Université de Bordeaux, INCIA, UMR5287, Bordeaux, France
[8] CEA, LIST, Diamond Sensors Laboratory, Gif-sur-Yvette, France
[9] Centre Hospitalier National d'Ophtalmologie des Quinze-Vingts, Paris, France
[10] Institute of Ophthalmology, University College London, London, UK
[11] Fondation Ophtalmologique Adolphe de Rothschild, Paris, France

E-mail: milan.djilas@inserm.fr

Abstract

Three-dimensional electrode geometries were proposed to increase the spatial resolution in retinal prostheses aiming at restoring vision in blind patients. We report here the results from a study in which finite-element modeling was used to design and optimize three-dimensional electrode geometries. Proposed implants exhibit an array of well-like shapes containing stimulating electrodes at their bottom, while the common return grid electrode surrounds each well on the implant top surface. Extending stimulating electrodes and/or the grid return electrode on the walls of the cavities was also considered. The goal of the optimization was to find model parameters that maximize the focalization of electrical stimulation, and therefore the spatial resolution of the electrode array. The results showed that electrode geometries with a well depth of 30 μm yield a tenfold increase in selectivity compared to the planar structures of similar electrode dimensions. Electrode array prototypes were microfabricated and implanted in dystrophic rats to determine if the tissue would behave as hypothesized in the model. Histological examination showed that retinal bipolar cells integrate the electrode well, creating isolated cell clusters. The modeling analysis showed that the stimulation current is confounded within the electrode well, leading to selective electrical stimulation of the individual bipolar cell clusters and thereby to electrode arrays with higher spatial resolution.

(Some figures in this article are in colour only in the electronic version)

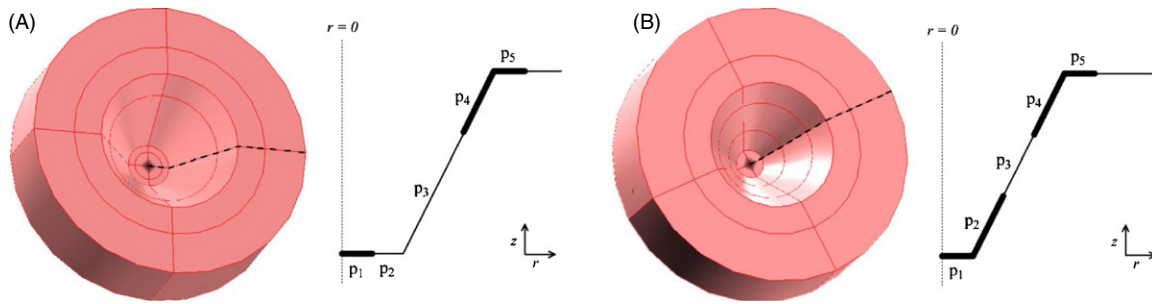[12] Author to whom any correspondence should be addressed.

Figure 1. 3D electrode geometries and their corresponding half cross sections. The dashed lines in the 3D representations mark geometry half cross sections. Each electrode half cross section is defined with five parameters (p_1–p_5) which represent the lengths of the segments. Cavity wall inclination is 54.7° for both geometries. Active electrode segments (thick lines in the half cross sections) are separated by insulated segments (thin lines in the half cross sections).

1. Introduction

In normal-sighted individuals, vision begins when light enters the eye and hits photoreceptor cells in the retina. The role of these cells is to convert light into bioelectric signals which are subsequently processed by complex inner retinal circuitry. Processed visual information is eventually encoded in the form of electric impulse trains that are sent to the brain via the optic nerve. In the cases of retinal degeneration caused by diseases like age-related macular degeneration and retinitis pigmentosa, the number of photoreceptor cells is significantly reduced, causing a reduction of visual acuity and, in worst cases, complete blindness. Following photoreceptor degeneration, parts of the inner layers of the retina, including bipolar and ganglion cells, remain (Humayun *et al* 1996, 1999). While several strategies, such as gene therapy (Bainbridge *et al* 2008, Maguire *et al* 2008) and neuroprotection (Frasson *et al* 1999, Takeuchi *et al* 2008, Tao *et al* 2002), aim at preventing photoreceptor degeneration, the concept of retinal electrical prostheses has been developed to restore useful vision in blind patients by activating the remaining inner retinal network (Shannon 1992). The system can either consist of an implanted stimulating device coupled with an external camera and a coding device (Weiland *et al* 2005) or all these functions can be integrated into a single chip (Zrenner 2002). Eventually the recorded image is encoded into an electrical pattern and sent to the dystrophic retina using a stimulation electrode array.

To activate the dystrophic retina, different approaches have been proposed. Sub-retinal stimulation with implants at the original site of photoreceptors aims at activating bipolar cells (Zrenner 2002), whereas epi-retinal stimulation with implants in the vitreous body on the inner limiting membrane aims at stimulating retinal ganglion cells (Humayun *et al* 2003, Rizzo *et al* 2003).

In neuroprostheses, the resolution of individual electrodes remains a general and important challenge. This question is particularly important in retinal prostheses to improve the quality of the images mapped onto an electrode array. Planar electrode arrays show limited activation selectivity of cells underlying the electrode array (Winter *et al* 2007). Different strategies have been developed to increase stimulation specificity. Bipolar stimulations with concentric electrodes were found to restrict positive currents to the center and generate opposite currents on the edges. This strategy requires

increasing the number of electrodes and therefore packing a larger number of electrode leads in a limited space. To remove this obstacle, a common return electrode in the form of a grid that surrounds all stimulating electrodes can be used. The increase in the stimulation resolution was recently quantified in a modeling study considering all configurations (Joucla and Yvert 2009). Three-dimensional electrode arrays were also proposed to decrease inter-electrode cross-talk and provide improved bio-electronic interfacing. Previous studies reported that migration of cells occurs around or within the 3D-structures of stimulating electrodes (Butterwick *et al* 2009, Loudin *et al* 2007, Palanker *et al* 2004a, 2004b, 2005). Butterwick *et al* even investigated on animals the minimum opening size for cells to enter into an implant cavity.

To define which shape of 3D structure would provide the best localization of electric current, we first produced finite-element models of three-dimensional electrode geometries with well-like shapes, and then optimized them to find model parameters that maximize stimulation focalization in the specific area where bipolar cells are located. The objective was increasing current density between the stimulating and return electrodes inside the wells and reducing it outside these zones. To verify our starting hypothesis that retinal bipolar cells, but not reactive glial cells, would migrate into and integrate with the 3D structures, 3D implant prototypes were microfabricated and implanted into the subretinal space of blind rats. A histological analysis was subsequently performed.

2. Methods

2.1. Modeling and optimization

Two implant models were considered and implemented in this study. They consist of a conductive plane in which there is a cavity. The stimulating electrode is at the bottom of the cavity, whereas the contra-electrode is a conductive plane surrounding the cavity. These two active electrode surfaces are separated by insulating sidewalls inside the cavity. Both electrode structures are axially symmetric and can thus be defined by their half cross sections (figure 1). The two models differ in the arrangement and the active and insulating surfaces inside the cavity. In configuration A, the stimulating electrode does not cover the entire cavity bottom; there is an insulating section between the stimulating electrode and the cavity sidewall. In
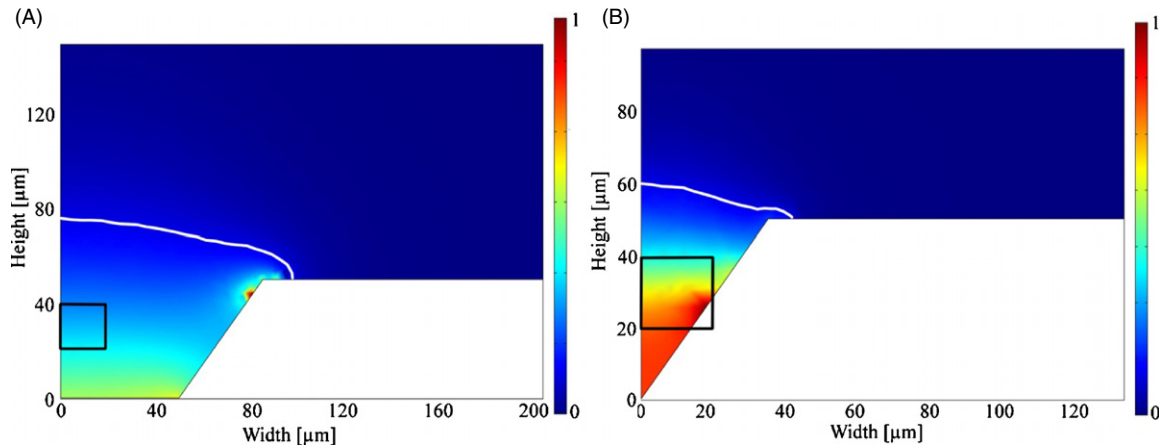
Figure 2. Current density distributions in the vicinity of the cavity for configurations A (left) and B (right) for one iteration in the optimization with cavity depth of 50 μm. White contours mark 10% of maximal current density. Black squares are the stimulation targets. Color bars are normalized. 10 μA are injected through the stimulating electrode in both cases.

configuration B, the stimulating electrode covers the entire cavity bottom and extends onto the lower part of the cavity wall. In both configurations, the contra-electrode extends from the top surface onto the sidewalls in the cavity.

The half cross sections can be defined using five parameters, p_1–p_5, which are the lengths of individual segments constituting the model geometries. Electrically active electrode surfaces are the thick segments, while the insulating surfaces are the thin segments. The different electrode configurations are illustrated in figure 1. For configuration A, these five parameters are: (A1) stimulating electrode radius, (A2) distance from stimulating electrode edge to the cavity sidewall, (A3) the length of the insulating segment on the cavity sidewall, (A4) the length of the contra-electrode segment that extends onto the cavity sidewall and (A5) the length of the horizontal segment of the contra-electrode. For configuration B, these five parameters are: (B1) the length of the horizontal segment of the stimulating electrode, (B2) the length of the stimulating electrode segment that extends onto the cavity sidewall, (B3) distance from the stimulating electrode to the contra-electrode, (B4) the length of the contra-electrode segment extending onto the cavity sidewall and (B5) the length of the horizontal segment of the contra-electrode. In the first instance, the electrodes were later microfabricated using a classical silicon wet etching process which is why the inclination of the cavity sidewall was fixed to the etching angle (54.7°) for (1 0 0) silicon.

Finite-element models were created using the Comsol Multiphysics Modeling and Simulation software package (Comsol AB). The physical model used in the simulations was the two-dimensional axially symmetric DC conductive media model, defined by the following relationships:

$$\mathbf{J} = \sigma\mathbf{E},$$
$$\nabla\mathbf{J} = Q,$$
$$Q = -\nabla(\sigma\nabla V),$$

where $\mathbf{J}$ is the current density vector, $\mathbf{E}$ is the electric field vector, σ is the electric conductivity of the media, Q is the electric charge and V is the electric potential.

Each segment in the electrode model was assigned a particular boundary condition. For the segments that constituted the stimulating electrode, it was inward current flow. Current density was set to correspond to the current intensity of 10 μA divided by the stimulating electrode area. In order not to overestimate electrode selectivity, the contra-electrode was not modeled as an ideal ground, but instead with a distributive resistance at a zero potential. If the contra-electrode were modeled with zero resistance, all the current injected from the stimulating electrode would be recuperated at the closest edge of the contra-electrode, which would not be realistic. Contra-electrode electric conductivity was set to 338 S m^{-1}, corresponding to the value found experimentally in a previous study (Joucla and Yvert 2009). Apart from the stimulating electrode and contra-electrode, all other segments of the model were defined as electric insulation. Current density distributions were computed in a rectangular sub-domain $D = [0, 300\ \mu\text{m}] \times [0, 600\ \mu\text{m}]$. The electrical resistivity of the sub-domain was set to 50 Ω m to approximate the electric resistivity of the remaining layers in the degenerated retina (Zhou and Greenberg 2009).

Electrode geometries were optimized using MATLAB (The Mathworks) to find optimal model parameters that yield the best stimulation selectivity. Electrode geometry was considered optimal if a set of model parameters produced the highest concentration of current in the target of stimulation, defined as a rectangular area $T = [0, 20\ \mu\text{m}] \times [20\ \mu\text{m}, 40\ \mu\text{m}]$, shown in figures 2(A) and (B). These values were chosen to approximately match the location of the remaining functional cells targeted for stimulation (Famiglietti 1981, Wassle and Boycott 1991), also taking into account that a glial layer would eventually cover the dystrophic retina. Maximizing the current density integral inside this region is equivalent to maximizing the voltage drop between the soma and the synaptic terminal of the bipolar cells and thus provides higher terminal depolarization (Gerhardt *et al* 2010). Selectivity was quantified by dividing the surface integral of the norm of the current density vector inside the stimulation

Table 1. Optimization parameter ranges.

		p_1 (μm)	p_2 (μm)	p_3 (μm)	p_4 (μm)	p_5 (μm)
Planar structure	Initial value	5	5	0	0	5
	Step	5	5	N/A	N/A	5
	Final value	50	50	N/A	N/A	30
Configuration A	Initial value	5	0	0	0	5
	Step	5	2	2	2	5
	Final value	50	10	50	50	30
Configuration B	Initial value	0	0	0	0	5
	Step	5	2	2	2	5
	Final value	50	50	50	50	30

For horizontal segments, the values represent the segment length. For inclined segments, the values represent the lengths of their *z*-axis projections. For configuration A, the horizontal segments are p_1, p_2 and p_5; the rest constitute the sidewall. For configuration B, the horizontal segments are p_1 and p_5; the rest are inclined.

target zone by the surface integral of the norm of the current density vector outside this area:

$$\text{Selectivity} = \frac{\iint_T \|\mathbf{J}\| \, dT}{\iint_{D/T} \|\mathbf{J}\| \, d(D/T)}.$$

For the purposes of later comparison, optimization was additionally performed for a planar structure, which was defined as configuration A, but with parameters p_3 and p_4 set to zero. Parameter ranges and step increments between iterations are listed in table 1. Optimizations were performed under the additional constraints that (1) the fabrication mask openings, corresponding to the electrically active electrode surfaces, must be at least 5 μm apart, and (2) the depth of the cavity does not exceed 50 μm.

2.2. Experimental validation

The above models rely on the hypothesis that retinal neurons migrate into the implant cavities. To validate this hypothesis, implant prototypes with wells were microfabricated and implanted subretinally into three transgenic P23H rats at an age when photoreceptor degeneration is complete. Eventually histological staining was performed to check whether cells have indeed migrated into the implant wells. In the following, we give more details of each step in the experimental validation.

Implant prototypes with optimized parameters corresponding to the well depth of 30 μm and the well diameter of 30 μm (measured at the electrode array common plane level) were fabricated. Only electrode substrates on polyimide were made, without any electrically active surfaces.

The surgical procedure used to implant these prototypes was described in detail previously (Salzmann *et al* 2006). Briefly, P23H blind rats were anesthetized by intramuscular injection with a 4:1 mixture of ketamine–xylazine (ketamine 100 mg kg^{-1}, xylazine 10 mg kg^{-1}) (Ketamine 500: Virbac, Carros, France; xylazine 2%: Rompun®, Bayer Pharma, Puteaux, France). A small radial sclerotomy was made 1.5 mm behind the limbus with a 25G needle. Biolon® (1% sodium hyaluronate, Bio-Technology General, Rehovot, Israel) was injected into the subretinal space through the sclerotomy in

order to obtain a localized retinal detachment. After inducing a retinal detachment, the implant was inserted into the subretinal space. The correct position of the implant was controlled *in vivo* with indirect ophthalmoscopy.

After at least a month, animals were anesthetized, sacrificed and perfused with fixative (4% wt/vol) paraformaldehyde in phosphate buffered saline (PBS; 0.01M, pH 7.4) in order to maintain the implant at its position and limit displacement during the histological procedure. Eye cups were then fixed overnight at 4 °C with the same fixative. The tissue was cryoprotected in successive solutions of PBS containing 10%, 20% and 30% sucrose at 4 °C, and embedded in NEG50® (Microm Microtech France, Francheville, France) Eye-cup cryo-sections (10 μm thickness) were permeabilized for 5 min in PBS containing 0.1% Triton X-100 (Sigma, St Louis, MO), rinsed and incubated in PBS containing 1% bovine serum albumin (Sigma) and 0.05% Tween 20 (Sigma) for 1 h at room temperature. The primary antibodies directed against GFAP (rabbit, 1/400, Dako) and Goα (mouse, 1:200, Chemicon) were added to the solution overnight at 4 °C. Sections were rinsed and then incubated with the secondary antibody, goat anti-rabbit IgG or goat anti-mouse IgG conjugated to either Alexa TM594 or Alexa TM488 (1:500, Molecular Probes) for 2 h at room temperature. Cell nuclei were revealed with 4′,6-diamidiphenyl-indole (DAPI), which was added during the final incubation period. Sections were rinsed, mounted with Fluorsave reagent (Calbiochem) and viewed with a microscope (LEICA DM 5000B) equipped with a Ropper scientific camera (Photometrics cool SNAP TM FX).

3. Results

3.1. Mathematical model

The well shapes modeled in this paper are illustrated in figure 1 (see section 2). The well wall has an inclination of 54.7 °, which corresponds to the angle obtained during silicon etching. Our aim was to define the optimum configurations and parameters generating the highest current densities in the stimulation target (black square in figure 2). This stimulation target corresponds to a 20 μm thick cylinder situated at 20 μm from the bottom of the well at the exact position where bipolar
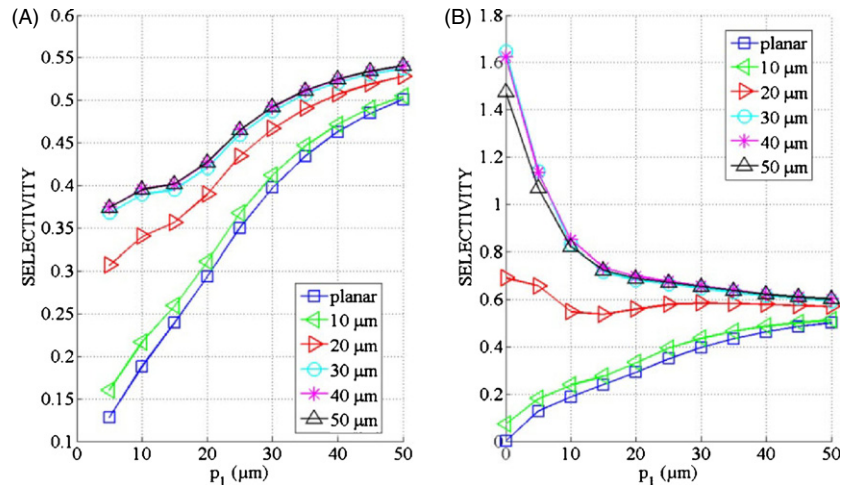
Figure 3. Comparison of selectivity for geometry A (left) and B (right) over a range of cavity depths and a range of values of parameter p_1. The figure legends indicate cavity depth.

cells to be stimulated are expected to lay. In configuration A, the stimulating electrode is at the bottom of the well (parameter p_1) surrounded by an isolating layer (p_2), while the returning grid is at the surface of the implant (p_5), which can be extended on the descending well wall (parameter p_4). In configuration B, the stimulating electrode and the returning grid can both extend on the well wall with parameters p_2 and p_4, respectively. The examples of current density distributions for the two electrode configurations are illustrated in figure 2. Optimal stimulation parameters (p_1–p_5, figure 1) were the ones that produced the maximal stimulation selectivity, defined previously (see section 2). Maximal electrode selectivity for configuration A for a range of cavity depths and stimulating electrode sizes is shown in figure 3. For comparison purposes, the plots also include the selectivity computed for the optimal planar structure. For configuration A, selectivity rises with the increased size of the stimulating electrode (parameter p_1 in figure 1(A)). For configuration B, due to the extension of the stimulation electrode on the cavity walls (parameter p_2 in figure 1(B)), maximal selectivity decreases with the increased radius of the cavity bottom surface (parameter p_1 in figure 1(B)). For both electrode configurations, selectivity improves with increased cavity depth. With depths up to 20 μm (corresponding to the lower edge of the stimulation target zone), there is little difference between the two configurations; there is also little improvement in selectivity compared to the planar electrode geometry. Electrode selectivity reaches its peak at the depth of 30 μm for both configurations. Configuration B yields better selectivity than configuration A for all stimulating electrode sizes. The difference is most prominent for smaller stimulating electrode sizes, e.g. for $p_1 = 5$ μm, there is approximately a threefold increase in selectivity when optimal geometry B is compared to optimal geometry A, and a tenfold increase when optimal geometry B is compared to the optimal planar electrode structure (figure 3).

To eventually pack as many electrodes as possible in a limited space, it is of interest to have parameters p_1 and p_5 as small as possible. This will result in having the minimal size

of a single electrode and therefore also the minimal center-to-center inter-electrode distance in an array. The effect of perturbation of these two parameters (p_1 and p_5) on overall electrode selectivity was investigated. Parameter p_1 was varied in the range given in table 1, while the other four parameters were kept fixed at their optimal values. The same procedure was repeated for parameter p_5. For configuration A, changing the stimulating electrode size had only a slight influence on selectivity, while increasing parameter p_1 for configuration B significantly degraded it (figure 4, left). The perturbation of parameter p_5 showed little effect on selectivity for both configurations (figure 4, right).

3.2. Experimental validation

The above models rely on the hypothesis that retinal neurons are located in the implant cavity. To determine if retinal neurons indeed enter into the wells, implant prototypes with wells were microfabricated (figure 5). A circular shape of the cavity (viewed from top) was not feasible using silicon molds. Instead, the effective geometry was eventually realized having a square cross section (figure 5(D)). When inserted into the subretinal space, their correct positioning was controlled *in vivo* by examining the eye fundus. Figure 6 illustrates an implant prototype in the subretinal space with retinal blood vessels clearly seen above. When eye sections were immunolabeled for glial cells with a GFAP antibody, and for retinal ON bipolar cells with a Goα antibody, a glial layer was found to cover the cavity, while bipolar cells were also found inside the implant cavities (figure 7). The number of such neuronal cells migrating into 30 μm implant wells was counted and the ratio between bipolar cells and the total number of cells bodies computed. The numbers are listed in table 2 and illustrated in figure 8(B). These observations confirmed that retinal neurons do fall into the implant cavities as hypothesized in the model study.
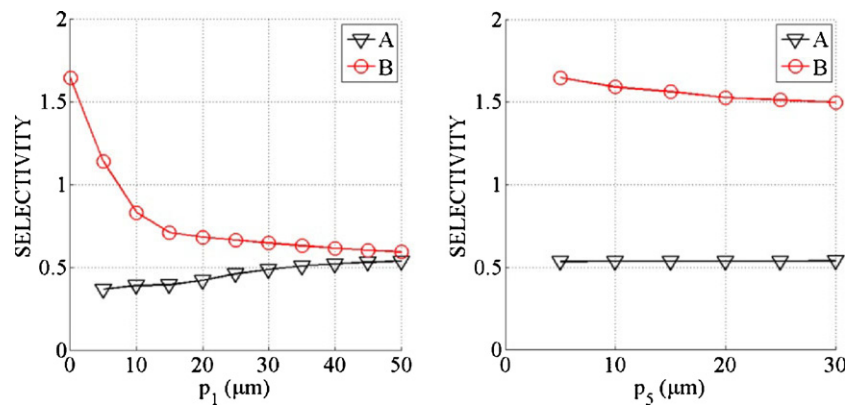
Figure 4. Influence of parameter perturbation on electrode selectivity for electrode geometries (A) and (B). Each point is computed using optimal model parameters and fixed values for parameters p_1 (left) and p_5 (right) for a fixed cavity depth of 30 μm.
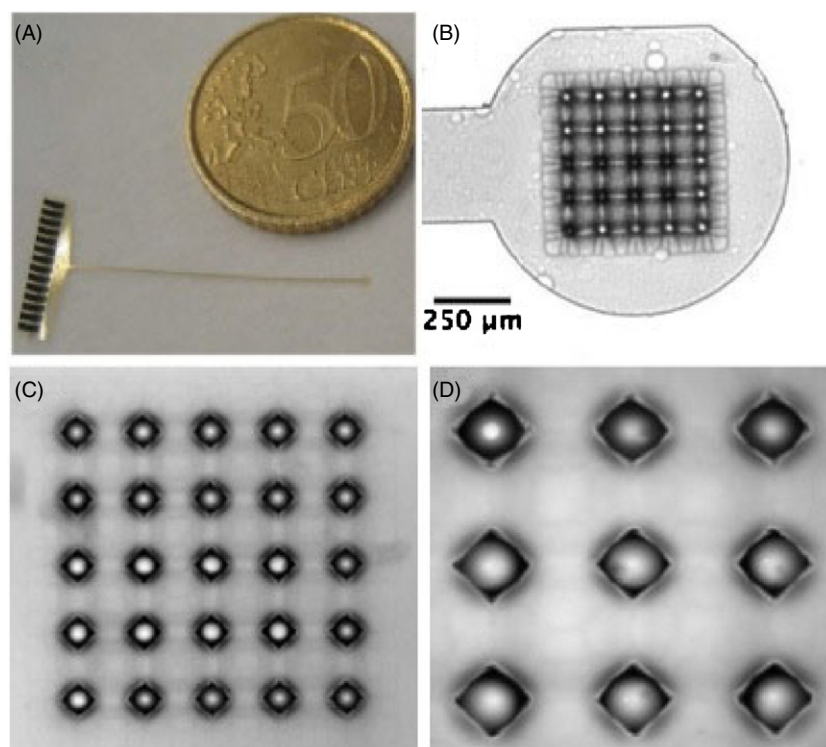

Figure 5. Microfabricated polyimide implant. (A) The whole implant shown together with a 50 eurocent coin for size reference. (B)–(D) Close-ups of the electrode array.
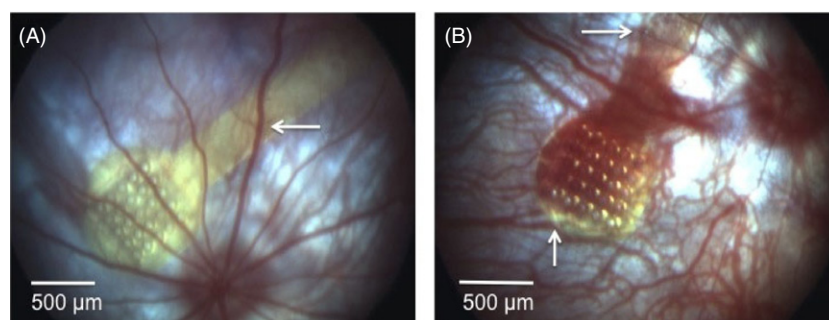

Figure 6. Endoscopic control of the implant position 1 week after surgery. Blood vessels of the retina passing over the implant (horizontal arrows on (A) and (B)) and of choroidal vessels under the implant (vertical arrows on (B)) indicate proper sub-retinal implant placement.
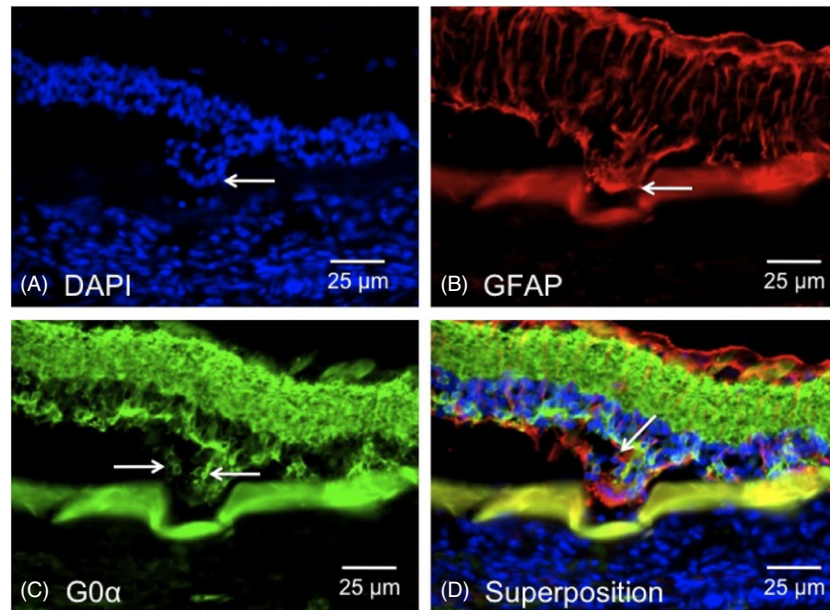
Figure 7. Neuronal integration of the P23H rat retina in a 3D retinal implant well. (A) DAPI nuclear staining showing the cell nuclei integrating the well (A, arrow). (B) GFAP immunolabeling showing the absence of a major retinal gliosis at the site of integration in retinal implant well. (C) Goα immunolabeling to visualize ON bipolar cells integrated into the implant well (arrows). (D) Superposition of images to illustrate the respective position of all the cells.
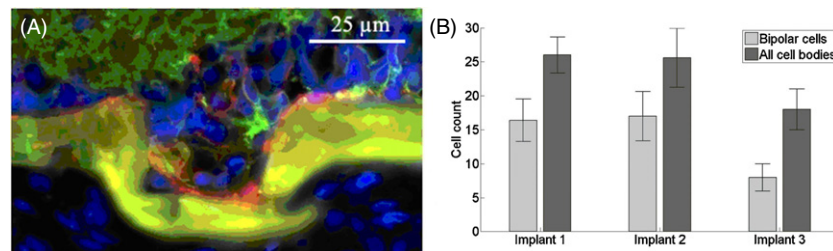

Figure 8. (A) Close-up showing the neuronal integration of the P23H rat retina into a 30 μm implant well. (B) Evaluation of the number of cells migrating into the electrode array wells in three implanted rats. Numbers of the bipolar cells and all cell bodies, together with their ratios, are given in table 2.

Table 2. Number of cells inside implant wells.

Implant	Bipolar cells	All cell bodies	Ratio
1	16.4 ± 3.1	26.0 ± 2.6	63%
2	17.0 ± 3.6	25.6 ± 4.3	66%
3	8.0 ± 2.0	18.0 ± 3.0	44%

Means and standard deviations of the number of cells per electrode well.

4. Discussion

High stimulation selectivity is obtained by placing an active and a return electrode close to each other producing a zone of high current density, and at the same time having very little current outside this area. The tradeoff of having the electrical fields confined in wells is that cells located in between pixels (between neighboring electrodes and outside any well) remain out of reach of the electrical stimulation.

Palanker and colleagues first demonstrated that the retinal tissue can mold itself around the 3D-shapes with cells even migrating through a perforated membrane (Palanker *et al* 2004a). However, this first study did not investigate the cell identity of the nuclei surrounding the 3D shapes or penetrating the perforated membranes. Therefore, these cells could have been glial or fibrotic cells multiplying to fill up empty cavities. A more recent study has shown that these cells are not glial cells (Butterwick *et al* 2009). The same study also concluded that cell bodies and neural processes integrate with the 3D implant configuration only when the voids are wider than approximately 10 μm. In our study, we investigated further how the retinal tissue can respond to the presence of 3D subretinal implants with cavities having a different geometry. With such implants, we confirmed that the tissue can mold itself into the 3D shapes. Furthermore, no major glial reaction was observed in contact with the polyimide implants. Instead, bipolar cell bodies were found localized in the well cavities. These bipolar cells were always separated from the implant by a glial cell layer. Indeed, following the photoreceptor degeneration, Muller glial cells forming the outer limiting membrane generate a continuous layer of processes at the outer surface of the retina. This layer generates an isolating layer which clearly prevents the transversal diffusion of ions

in the retinal, but instead favors the lateral diffusion at the implant surface. The fact that the dystrophic retinal tissue can integrate with the wells validates our hypotheses for the mathematical modeling of the electrical stimulation with the proposed implants. Moreover, the objective being to stimulate bipolar neurons, our aim to obtain the maximum current in a rectangle situated at a 20 μm distance in the tissue from the implant is consistent with the presence of the glial layer at the surface.

Different models were generated to optimize the efficiency of the electrical stimulation of neuronal tissues. These models demonstrated the interest of having a common returning grid electrode surrounding all stimulating electrodes (Joucla and Yvert 2009). Although 3D retinal implants were recently proposed, no model has investigated how the current would flow in the tissue depending on electrode geometry and the placement of active surfaces. In our study, we have limited our investigation to 3D implants showing wells containing the stimulating electrodes. In all cases, these 3D designs were more efficient than planar implants with a similar returning grid electrode. For configuration A, changing the stimulating electrode size had only a slight influence on selectivity, whereas increasing parameter p_1 for configuration B degraded it (figure 5, left). For the latter configuration it would therefore be of interest to choose the smallest values for p_1 as long as the maximal current density produced stays under a safe limit for a given electrode material. Platinum can safely deliver 0.35–0.4 mC cm^{-2} and iridium oxide has been shown to have a safe stimulation limit of up to 3–4 mC cm^{-2} (Beebe and Rose 1988). Even if the current density is within the safe limit for platinum, iridium oxide may still be a better choice in order to avoid parts of the metal with high current density (e.g. hot spot on return electrode in the left panel of figure 2) becoming inert after prolonged stimulation. As long as the electrodes are closer to the cell than the electrode size, smaller stimulating electrode sizes are also preferable in terms of reducing cell activation threshold (Sekirnjak *et al* 2006). In any cases, the current density will be higher between the stimulating electrode and the returning grid with unaffected surrounding areas, as originally proposed by Palanker *et al* (2004a). A potential issue with having parameter p_1 too small is that it may produce geometries with a cavity that might be too narrow. Indeed, if a pixel activates too few cells, its effect may not be perceived and thus visual perception may require multiple neighboring pixels stimulation as discussed in Loudin *et al* (2007). Thus, the small electrode size does not guarantee improved resolution. In the first instance, we have microfabricated and implanted electrodes with slightly wider cavities than optimal in order to examine how the retina interacts with the implant. Histological examination showed that the retinal tissue indeed migrates into the electrode array cavities (figure 8).

Little effect of parameter p_5 perturbation on selectivity (figure 4, right) implies that the stimulation current is always well confined inside the cavity and even the smallest contra-electrode ring around the cavity would be sufficient to eliminate inter-electrode crosstalk. This, together with having a small value for p_1, would allow the design of densely packed electrode arrays. Eventually the maximal number of electrodes will also depend on the tracks connecting each individual electrode to the electronic stimulator. Each lead must have a minimum width that needs to be taken into account when designing the implant.

Regarding the electrical conductivity of the retina, there may be a difference in values between the degenerated and healthy retina. In this study we have used values available in the literature for the healthy retina. However, retinal prostheses are eventually used to restore function in the cases of degenerated retina. After photoreceptors' death, the bipolar layer thickness decreases and the limiting inner membrane becomes thicker (Hood *et al* 2009). At present, to the best of our knowledge, there are no published data on the electrical conductivity of layers in degenerated retina.

The electrode–electrolyte interface is operating in a mode of reversible electrochemistry, which implies that charge injection per unit area is limited. In the areas of higher electric field, this capacitance will be exhausted first, after which current density will shift to other areas. Future work will also include the modeling of the distributed capacitive coupling between the tissue and implant.

Eventually, the electrodes will have to adapt to the human retina where the size of the cells will be comparable to the implant well size. In this case, a continuum bulk conductance model would be far from realistic and the effect on the bipolar cells will be exceedingly sensitive to the shape of the field on length scales smaller than the cell. The computational model would have to take this into account.

Finally, the purpose of this modeling study was to find an optimal geometry for stimulation electrode arrays for retinal prostheses, but the implants would eventually be applicable to neural prostheses in general, used for activating neural structures both in the central and peripheral nervous systems.

5. Conclusion

In our finite-element modeling study, 3D electrode geometries for retinal prostheses were designed and optimized with the goal to maximize electrode stimulation efficiency. Proposed electrode geometries have well-like structures with stimulating electrodes inside them, while electrical stimulation is facilitated by using a common return electrode surrounding each stimulating electrode in the array. The results show that electrode geometries with depths of 30 μm yield a tenfold increase in selectivity compared to the optimal planar structure of similar stimulating electrode dimensions. Histological examination validated the hypothesis that retinal tissue indeed migrates into electrode cavities, providing a more selective neuroelectric interface. The simulation shows that the injected stimulation current is confined within the electrode cavities, allowing for the activation of a smaller number of retinal cells by a single electrode in an array.

References

Bainbridge J W *et al* 2008 Effect of gene therapy on visual function in Leber's congenital amaurosis *N. Engl. J. Med.* **358** 2231–9

Beebe X and Rose T L 1988 Charge injection limits of activated iridium oxide electrodes with 0.2 ms pulses in bicarbonate buffered saline *IEEE Trans. Biomed. Eng.* **35** 494–5

Butterwick A, Huie P, Jones B W, Marc R E, Marmor M and Palanker D 2009 Effect of shape and coating of a subretinal prosthesis on its integration with the retina *Exp. Eye Res.* **88** 22–9

Famiglietti E V Jr 1981 Functional architecture of cone bipolar cells in mammalian retina *Vis. Res.* **21** 1559–63

Frasson M, Sahel J A, Fabre M, Simonutti M, Dreyfus H and Picaud S 1999 Retinitis pigmentosa: rod photoreceptor rescue by a calcium-channel blocker in the rd mouse *Nat. Med.* **5** 1183–7

Gerhardt M, Alderman J and Stett A 2010 Electric field stimulation of bipolar cells in a degenerated retina—a theoretical study *IEEE Trans. Neural Syst. Rehabil. Eng.* **18** 1–10

Hood D C, Lin C E, Lazow M A, Locke K G, Zhang X and Birch D G 2009 Thickness of receptor and post-receptor retinal layers in patients with retinitis pigmentosa measured with frequency-domain optical coherence tomography *Invest. Ophthalmol. Vis. Sci.* **50** 2328–36

Humayun M S, de Juan E Jr, Dagnelie G, Greenberg R J, Propst R H and Phillips D H 1996 Visual perception elicited by electrical stimulation of retina in blind humans *Arch. Ophthalmol.* **114** 40–6

Humayun M S *et al* 1999 Pattern electrical stimulation of the human retina *Vis. Res.* **39** 2569–76

Humayun M S *et al* 2003 Visual perception in a blind subject with a chronic microelectronic retinal prosthesis *Vis. Res.* **43** 2573–81

Joucla S and Yvert B 2009 Improved focalization of electrical microstimulation using microelectrode arrays: a modeling study *PLoS One* **4** e4828

Loudin J D *et al* 2007 Optoelectronic retinal prosthesis: system design and performance *J. Neural Eng.* **4** S72–84

Maguire A M *et al* 2008 Safety and efficacy of gene transfer for Leber's congenital amaurosis *N. Engl. J. Med.* **358** 2240–8

Palanker D *et al* 2004a Migration of retinal cells through a perforated membrane: implications for a high-resolution prosthesis *Invest. Ophthalmol. Vis. Sci.* **45** 3266–70

Palanker D, Vankov A, Huie P and Baccus S 2005 Design of a high-resolution optoelectronic retinal prosthesis *J. Neural Eng.* **2** S105–20

Palanker D V *et al* 2004b Attracting retinal cells to electrodes for high-resolution stimulation *Proc. SPIE* **5314** 306–14

Rizzo J F 3rd, Wyatt J, Loewenstein J, Kelly S and Shire D 2003 Perceptual efficacy of electrical stimulation of human retina with a microelectrode array during short-term surgical trials *Invest. Ophthalmol. Vis. Sci.* **44** 5362–9

Salzmann J *et al* 2006 Subretinal electrode implantation in the P23H rat for chronic stimulations *Br. J. Ophthalmol.* **90** 1183–7

Sekirnjak C, Hottowy P, Sher A, Dabrowski W, Litke A M and Chichilnisky E J 2006 Electrical stimulation of mammalian retinal ganglion cells with multielectrode arrays *J. Neurophysiol.* **95** 3311–27

Shannon R V 1992 A model of safe levels for electrical stimulation *IEEE Trans. Biomed. Eng.* **39** 424–6

Takeuchi K, Nakazawa M and Mizukoshi S 2008 Systemic administration of nilvadipine delays photoreceptor degeneration of heterozygous retinal degeneration slow (rds) mouse *Exp. Eye Res.* **86** 60–9

Tao W *et al* 2002 Encapsulated cell-based delivery of CNTF reduces photoreceptor degeneration in animal models of retinitis pigmentosa *Invest. Ophthalmol. Vis. Sci.* **43** 3292–8

Wässle H and Boycott B B 1991 Functional architecture of the mammalian retina *Physiol. Rev.* **71** 447–80

Weiland J D, Liu W and Humayun M S 2005 Retinal prosthesis *Annu. Rev. Biomed. Eng.* **7** 361–401

Winter J O, Cogan S F and Rizzo J F 3rd 2007 Retinal prostheses: current challenges and future outlook *J. Biomater. Sci. Polym. Ed.* **18** 1031–55

Zhou D D and Greenberg R J 2009 Microelectronic visual prostheses *Implantable Neural Prostheses 1* ed D Zhou and E Greenbaum (Berlin: Springer) pp 1–42

Zrenner E 2002 Will retinal implants restore vision? *Science* **295** 1022–5